Hot deformation behavior of a Sr-modified Al−Si−Mg alloy: Constitutive model and processing maps

Y. C. LIN[1,2,3], Shun-cun LUO[1,2], Xing-you JIANG[1,2], Yi TANG[1,2], Ming-song CHEN[1,2,3]

1. School of Mechanical and Electrical Engineering, Central South University, Changsha 410083, China;
2. Light Alloy Research Institute, Central South University, Changsha 410083, China;
3. State Key Laboratory of High Performance Complex Manufacturing,
Central South University, Changsha 410083, China

Abstract: Isothermal compression experiments were conducted to study the hot deformation behaviors of a Sr-modified Al−Si−Mg alloy in the temperature range of 300−420 °C and strain rate range of 0.01−10 s^{-1}. A physically-based model was developed to accurately predict the flow stress. Meanwhile, processing maps were established to optimize hot working parameters. It is found that decreasing the strain rate or increasing the deformation temperature reduces the flow stress. The high activation energy is closely related to the pinning of dislocations from Si-containing dispersoids. Moreover, the deformed grains and the Si-containing dispersoids in the matrix are elongated perpendicular to the compression direction, and incomplete dynamic recrystallization (DRX) is discovered on the elongated boundaries in domain with peak efficiency. The flow instability is mainly attributed to the flow localization, brittle fracture of eutectic Si phase, and formation of adiabatic shear band. The optimum hot working window is 380−420 °C and 0.03−0.28 s^{-1}.

Key words: Al−Si−Mg alloy; constitutive model; processing map; microstructure

1 Introduction

As one of the most useful modification approaches, thermo-mechanical forming has been usually used to eliminate the casting defects and change the microstructures [1]. Generally, the thermo-mechanical forming processes are very complex under different deformation conditions. The complicated hot deformation mechanisms, including strain hardening and dynamic softening, significantly affect the final microstructures and properties [2−7]. Thus, to acquire the products with desirable properties, optimizing the hot forming parameters and controlling the final microstructures are very important [8,9].

Al−Si−Mg alloy is widely applied in automotive and aerospace industries due to its excellent weldability, desirable wear resistance, and corrosion resistance. Up to now, some researchers have investigated the high-temperature flow behaviors of Al−Si−Mg alloys [10−12], and it is found that some inevitable casting defects, such as the shrinkage cavities and porosity, severely weaken the mechanical properties. Meanwhile, the brittle eutectic Si particles with acicular shape easily cause high localized stress concentration in the matrix, which may result in the nucleation and growth of voids.

The constitutive model is found to be an effective method to describe the change in mechanical response during hot deformation [1]. An accurate constitutive model can be embedded into the commercial FEM software for numerical simulation and analyzing the hot forming process. Thus, lots of constitutive models have been established to characterize the high-temperature flow behaviors of alloys in recent years. These models mainly include the physically-based models [13−16], phenomenological models [17−19], and artificial neural network models [20,21]. Additionally, the processing map, proposed by PRASAD et al [22] in terms of the

dynamic material model (DMM) theory, is a reasonable method to analyze hot workability and optimize forming parameters. From the processing map, the deformation mechanism can be reasonably interpreted, and the instable region related to flow instability can be well avoided [23−25].

Despite some investigations on the hot deformation behaviors and constitutive models for Al−Si−Mg alloys have been carried out, the developed constitutive equations are still not perfect enough to describe the entire complicated hot deformation process. Meanwhile, the high-temperature flow behaviors and processing map for the Al−Si−Mg alloy in homogenization state need the further study. In the present work, isothermal compression experiments are performed to research the hot deformation behaviors for a homogenized Al−Si−Mg alloy within broad scopes of strain rate and deformation temperature. A physically-based constitutive equation is developed to describe the hot deformation behaviors. Meanwhile, the hot forming parameters are optimized by establishing the processing map and the final microstructures are reasonably controlled.

2 Experimental

In the present work, die-cast Al−Si−Mg alloy is adopted with the chemical composition (mass fraction, %) of 7.70Si−0.31Mg−0.12Fe−0.12Ti−0.02Sr−(bal.)Al. Sr addition in as-cast Al−Si−Mg alloy is used to modify the eutectic Si morphology and dendrite arm spacing (DAS). Firstly, the received cast billet was homogenized at 540 °C for 8 h, followed by air cooling to room temperature. Thus, the soluble phases were completely dissolved. Then, cylinder specimens with 12 mm in height and 8 mm in diameter were cut from the homogenized cast billet. Before hot deformation, the microstructure of specimen was examined by optical microscope (OM) after being chemically etched with a solution of 10% HF and 5% HCl (volume fraction) in water. Figure 1 shows the microstructures of the homogenized Al−Si−Mg alloy. Obviously, some casting defects, including the shrinkage cavities and porosity, can be observed. In as-cast Al−Si alloys, the DAS was reported to have greater effect on strength compared with grain size. So, the DAS is measured from Fig. 1 with a mean value of 55 μm by linear intercept method. In addition, fine granular eutectic Si phases are uniformly distributed along the grain boundaries. Using the method mentioned in Ref. [11], the mean diameter and volume fraction of eutectic Si particles can be measured to be 3.1 μm and 11.05%, respectively. Meanwhile, a mass of Si-containing dispersoids marked by red dotted line appear in α(Al) matrix. This phenomenon was also discovered in other Al−Si−Mg alloy during solution

treatment [26]. Using the method mentioned in Ref. [26], the mean diameter and volume fraction of Si-containing dispersoids can be measured to be 320.26 nm and 13.86%, respectively. The isothermal compression experiments were carried out using a Gleeble 3500 thermal mechanical simulator. Four strain rates (0.01, 0.1, 1 and 10 s^{-1}) and four deformation temperatures (300, 340, 380 and 420 °C) were used in this work. Prior to loading, the samples were heated at a rate of 10 °C/s to the deformation temperature, and then held for 5 min to assure a homogeneous temperature field. All the specimens were instantly cooled in cold water to preserve the deformed microstructures when the height reduction reached 50%. The experimental data were automatically recorded by the test system during hot compression.
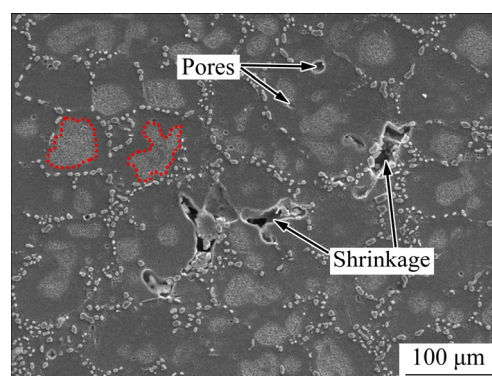

Fig. 1 SEM image of homogenized Al−Si−Mg alloy before hot deformation

3 Results and discussion

3.1 Flow stress analysis

Figure 2 shows the measured true stress−true strain curves of the homogenized Al−Si−Mg alloy from the isothermal compression experiments. Obviously, the flow stress is significantly affected by the deformation temperature, strain and strain rate. In the initial deformation stage, the work hardening due to the dislocation sliding, rapid proliferation and interaction leads to the quick increment of flow stress. With the strain further increasing, the dislocation density significantly increases, which results in the rapid increment of potential driving force of dislocation motion. Then, the dynamic recovery (DRV) and dynamic recrystallization (DRX) occur, which weaken the working hardening [27−29]. As a result, a platform is achieved. Subsequently, the flow stress slowly reduces to a stable state because the work hardening and flow softening become balanced dynamically. However, at low strain rate (0.01 s^{-1}) and low temperatures (300 and 340 °C), the flow stress decreases quickly. This may be attributed to the precipitation of fine Mg$_2$Si phases at low
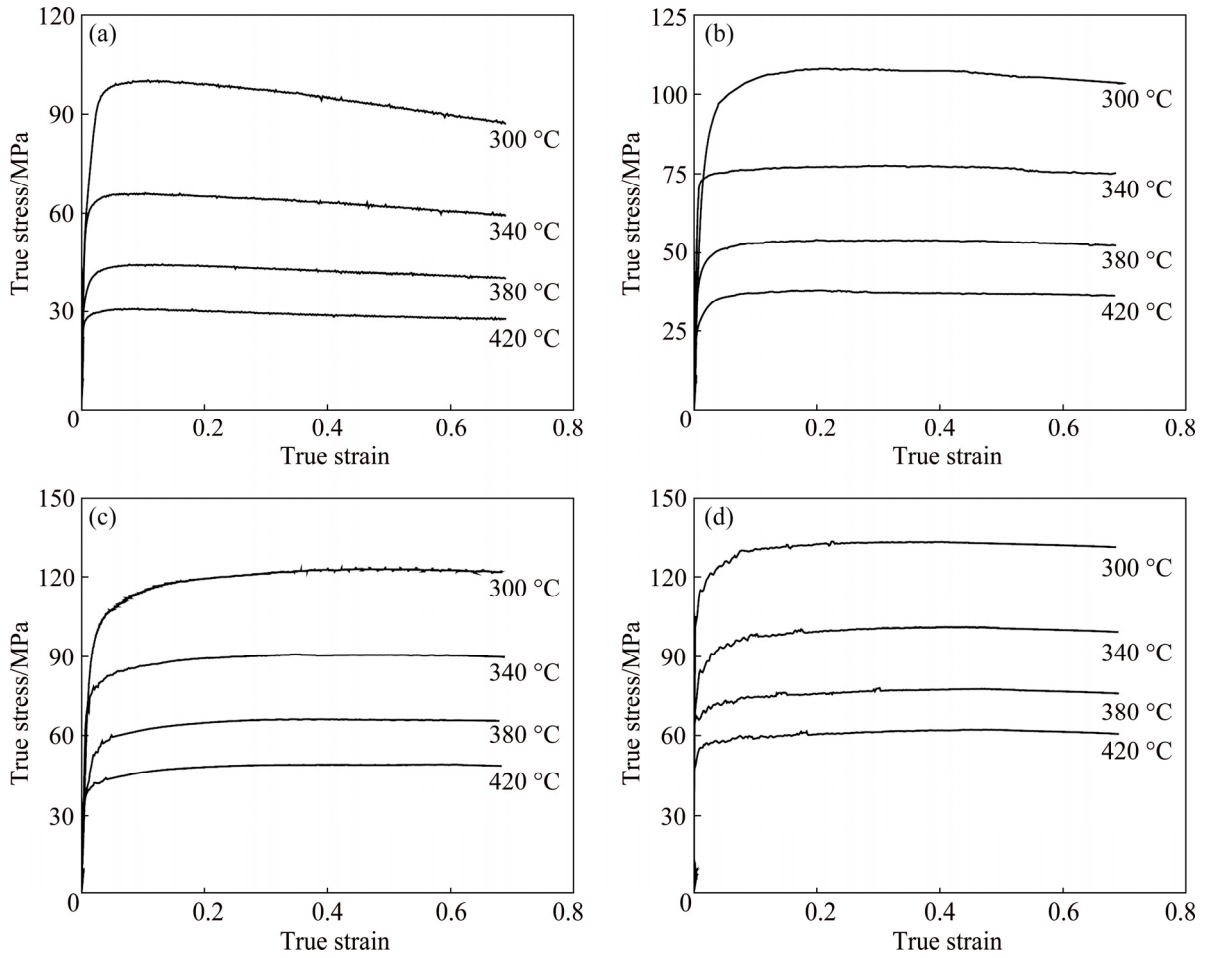
Fig. 2 True stress−strain curves of Al−Si−Mg alloy at different strain rates: (a) 0.01s^{-1}; (b) 0.1 s^{-1}; (c) 1 s^{-1}; (d) 10 s^{-1}

deformation temperatures. Also, the low strain rate allows more time for the coarsening and morphological variations of Mg$_2$Si phases from particle shape to planar shape during hot compression. So, the DRV is the primary softening mechanism of the homogenized Al−Si−Mg alloy.

3.2 New constitutive equations based on Estrin− Mecking and Avrami models

3.2.1 Estrin−Mecking model

Based on the Estrin−Mecking model [30], the strain hardening and dynamic recovery characteristics of alloys can be represented as

$$\sigma^{\mathrm{EM}} = \left[\sigma_{\mathrm{s}}^2 + \left(\sigma_{\mathrm{y}}^2 - \sigma_{\mathrm{s}}^2 \right) \exp\left(-2B\varepsilon\right) \right]^{1/2} \qquad (1)$$

where σ^{EM} refers to the flow stress; σ_{s} refers to the saturation flow stress; σ_{y} is the yield stress; B is the material constant associated with the Zener−Hollomon (Z) parameter.

Generally, the saturation stress (σ_{s}) can be obtained from the work hardening rate ($\theta = \mathrm{d}\sigma/\mathrm{d}\varepsilon$) and flow stress curve, as depicted in Fig. 3. Firstly, the point of inflection in $\theta - \sigma$ curve can be identified. Then, drawing
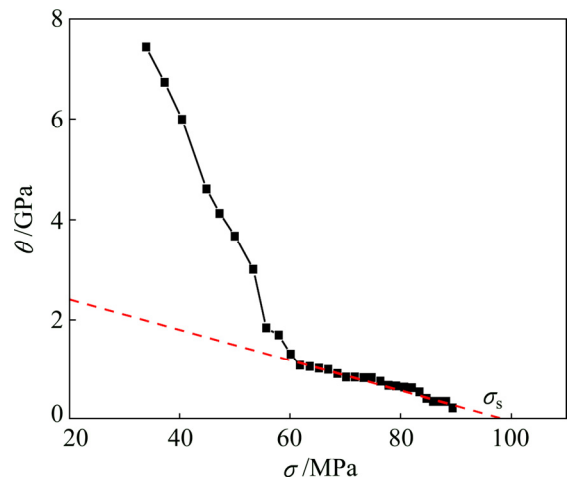

Fig. 3 Relationship between work hardening rate and flow stress

the tangent of $\theta - \sigma$ plot through the inflection point down to the horizontal axis, the horizontal intercept is considered as the value of the saturation flow stress. In addition, the yield stress (σ_{y}) under all tested conditions can be determined directly from the curves of stress− strain.

According to the Sellars−Tegart−Garofalo (STG) equation [31], the yield stress, saturation stress and steady-state stress can be expressed as

$$\sigma_y = \sigma_a + \delta_y \sinh^{-1}\left[\left(\frac{\dot{\varepsilon}\exp\left(\dfrac{Q}{RT}\right)}{A_y}\right)^{1/m_y}\right] \qquad (2)$$

$$\sigma_s = \delta_s \sinh^{-1}\left[\left(\frac{\dot{\varepsilon}\exp\left(\dfrac{Q}{RT}\right)}{A_s}\right)^{1/m_s}\right] \qquad (3)$$

$$\sigma_{ss} = \delta_{ss} \sinh^{-1}\left[\left(\frac{\dot{\varepsilon}\exp\left(\dfrac{Q}{RT}\right)}{A_{ss}}\right)^{1/m_{ss}}\right] \qquad (4)$$

where δ_y, A_y, m_y, δ_s, A_s, m_s, δ_{ss}, A_{ss} and m_{ss} are material constants, $\dot{\varepsilon}$ is the strain rate (s^{-1}), Q refers to the hot deformation activation energy (kJ/mol), R refers to the mole gas constant (8.31 J/(mol·K)), and T refers to the deformation temperature. While σ_a denotes the athermal stress, which is below the yield stress and unaffected by strain rate and deformation temperature. The variations of the yield stress with deformation temperature and strain rate are depicted in Fig. 4. From Fig. 4, the value of σ_a can be approximately identified to be 20 MPa.
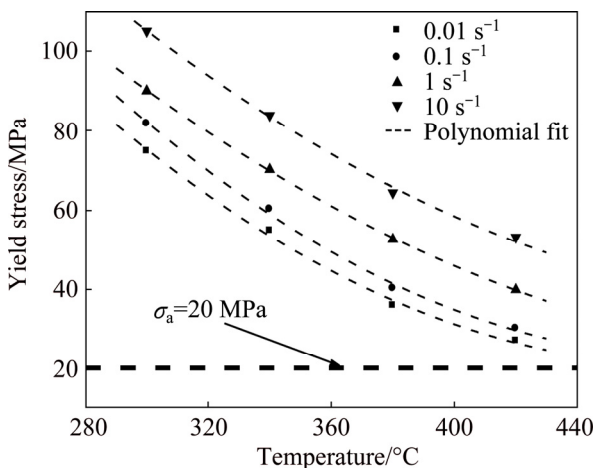

Fig. 4 Variations of yield stress values with deformation temperature and strain rate

It is widely believed that Z parameter can be applied to represent the influence of deformation temperature and strain rate on high-temperature flow behaviors:

$$Z = \dot{\varepsilon}\exp[Q/(RT)] \qquad (5)$$

Using the method mentioned in Ref. [32], the activation energy Q can be estimated to be 392.760 kJ/mol, which is greater than that of the solutionized Al−Si−Mg alloy reported in Ref. [33]. This difference is mainly because a large amount of Si-containing dispersoids in the α(Al) matrix can dramatically pin dislocations and contribute in the form of Orowan stress during hot deformation. Then, the dislocation density is significantly increased, which leads to the large deformation resistance. As a result, activation energy Q is very high (>300 kJ/mol). For the homogenized Al−Si−Mg alloy, the DRV is the primary softening mechanism during hot deformation. Also, the DRV is a thermal activated process. So, the high activation energy during hot deformation reflects the thermal activation energy needed for DRV.

Based on the experimental flow stress data, the different material parameters involved in Eqs. (2)−(4) can be determined by L−M optimization algorithm, as listed in Table 1. Then, according to the STG model, the yield stress can be described as a function of Z parameter, as plotted in Fig. 5. From Fig. 5, it can be observed that the experimental yield stresses are within a scatter band of ±6 MPa around the predicted results. Similar conclusions have been obtained from the relationship between the saturation/steady-state stresses and Z parameter. These conclusions indicate that the athermal stress of about 20 MPa can provide a satisfactory prediction of yield stress. Therefore, the yield stress, saturation stress and steady-state stress of the studied Al−Si−Mg alloy can be expressed as

$$\begin{cases} \sigma_y = 20 + 14.7629\sinh^{-1}\left[\left(\dfrac{Z}{8.4528\times10^{28}}\right)^{1/3.7}\right] \\[2mm] \sigma_s = 50.8037\sinh^{-1}\left[\left(\dfrac{Z}{2.2791\times10^{29}}\right)^{1/8.83}\right] \\[2mm] \sigma_{ss} = 47.2266\sinh^{-1}\left[\left(\dfrac{Z}{2.2522\times10^{29}}\right)^{1/8.29}\right] \\[2mm] Z = \dot{\varepsilon}\exp\left(\dfrac{392760}{RT}\right) \end{cases} \qquad (6)$$

Then, only the material constant B in Eq. (1) needs to be identified. Based on the strains and corresponding flow stresses in the period of strain hardening and dynamic recovery, the material constant B under all the tested conditions can be determined by linear regressing $\ln(\sigma_s^2 - \sigma^2)$ versus ε plots. Figure 6 depicts the relations of the material constant B and Z parameter. Obviously, the material constant B slowly increases with the increase of Z parameter at the strain rates of 0.01 and 0.1 s^{-1}, while rapidly increases at the strain rates of 1 and

Table 1 Optimized values of material parameters

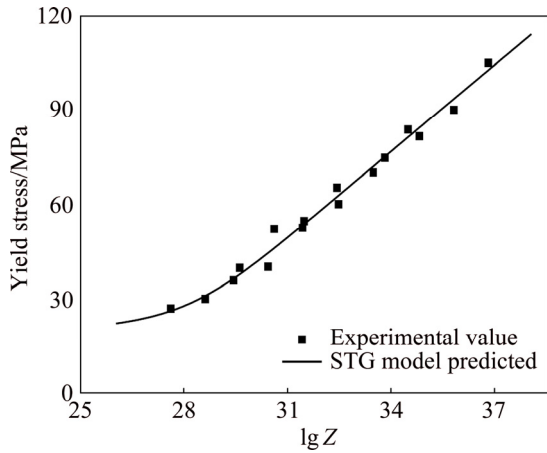| δ_y/MPa	A_y	m_y
14.7629	8.4528×10^{28}	3.7
δ_s/MPa	A_s	m_s
50.8037	2.2791×10^{29}	8.83
δ_{ss}/MPa	A_{ss}	m_{ss}
47.2266	2.2522×10^{29}	8.29

Fig. 5 Variations of yield stress values with Zener−Hollomon parameter
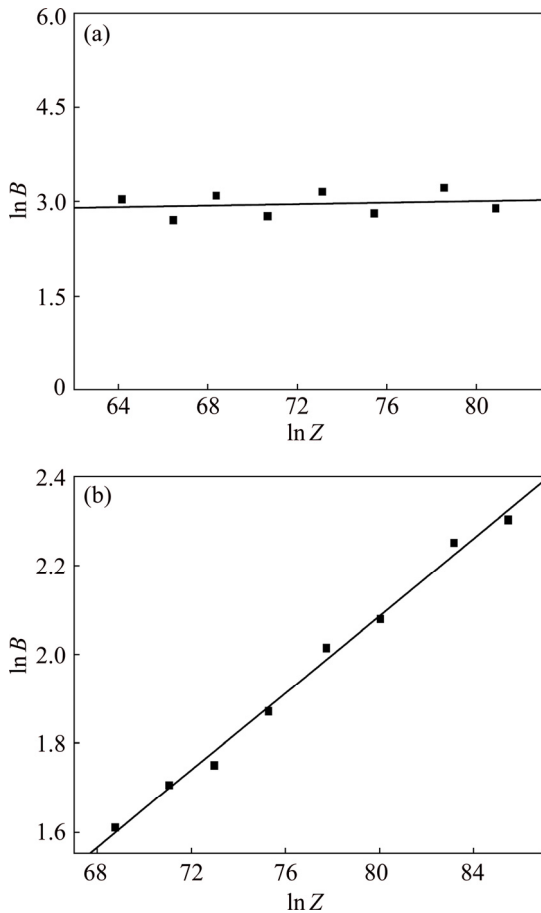

Fig. 6 Relationship between material constant B and Z parameter: (a) $\dot{\varepsilon}$ =0.01 and 0.1 s^{-1}; (b) $\dot{\varepsilon}$ =1 and 10 s^{-1}

10 s^{-1}. Thus, the material constant B can be expressed as

$$B=\begin{cases} 12.6635Z^{0.0058} \left(\dot{\varepsilon}=0.01 \text{ and } 0.1 \text{ s}^{-1}\right) \\ 0.2496\,Z^{0.0434}\left(\dot{\varepsilon}=1 \text{ and } 10 \text{ s}^{-1}\right) \end{cases} \tag{7}$$

According to Eq. (1), the flow behavior only up to the peak strain, where the strain hardening and dynamic recovery are the main factors affecting the flow stress, can be described by the Estrin−Mecking model. Therefore, the effects of flow softening need to be incorporated into the constitutive equation when the strain is beyond the peak strain.

3.2.2 Incorporation of Avrami equation

For compensating the softening effects induced by DRX, the DRX volume fraction should be determined at every strain which is larger than the critical strain for DRX, and can be estimated by [34]

$$X=\frac{\sigma^{\mathrm{EM}}-\sigma}{\sigma_s-\sigma_{ss}} \tag{8}$$

where σ^{EM} denotes the flow stress calculated by Eq. (1) and σ_{ss} is the steady state flow stress. According to the Avrami model [35], the volume fraction of DRX can be calculated by

$$X=1-\exp\left[-a\left(\varepsilon-\varepsilon_c\right)^b\right] \tag{9}$$

where a and b are material constants, and ε_c is the critical strain.

Generally, critical strain ε_c is not easy to be precisely determined under different deformation conditions for the studied Al−Si−Mg alloy. Thus, similar to other work [36], the critical strain ε_c in Eq. (9) is replaced by the peak strain ε_p. Using the method mentioned in Refs. [1,36], the peak strain ε_p can be expressed as a function of Z parameter:

$$\varepsilon_p=0.0068Z^{0.0468} \tag{10}$$

The values of material constants a and b under all the tested conditions can be determined by linear regressing $\ln(-\ln(1-X))$ versus $\ln(\varepsilon-\varepsilon_c)$ plots.

Figure 7 depicts the relationship between the material constants a, b and Z parameter. Obviously, with the increase of Z parameter, the material constant a slowly increases, while the material constant b slowly decreases. Thus, the material constants a and b can be expressed as the functions of Z parameter, respectively:

$$a=2.0362Z^{0.0175} \tag{11}$$

$$b=3.6676Z^{-0.0083} \tag{12}$$

Therefore, the developed constitutive models based on the Estrin−Mecking model and Avrami equation can be summarized as
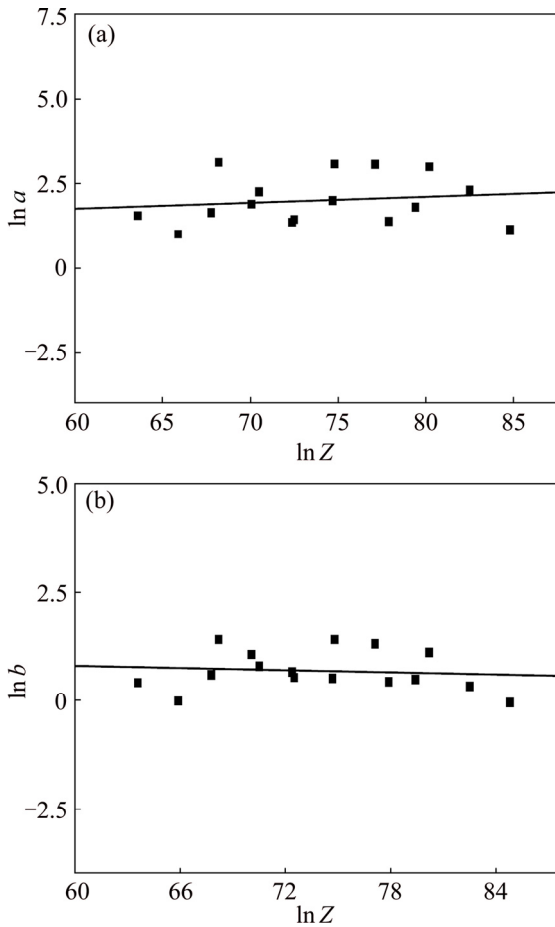
Fig. 7 Relationship between material constants a (a), b (b) and Z parameter

$$\begin{cases} \sigma^{\mathrm{EM}} = \left[\sigma_{\mathrm{s}}^2 + \left(\sigma_{\mathrm{y}}^2 - \sigma_{\mathrm{s}}^2 \right) \exp\left(-2B\varepsilon \right) \right]^{1/2}, \quad \varepsilon < \varepsilon_{\mathrm{p}} \\[2mm] \sigma = \sigma^{\mathrm{EM}} - \left\{ 1 - \exp\left[-a\left(\varepsilon - \varepsilon_{\mathrm{c}} \right)^b \right] \right\} \left(\sigma^{\mathrm{EM}} - \sigma_{\mathrm{ss}} \right), \quad \varepsilon \geq \varepsilon_{\mathrm{p}} \\[2mm] \sigma_{\mathrm{y}} = 20 + 14.7629 \sinh^{-1}\left[\left(\dfrac{Z}{8.4528 \times 10^{28}} \right)^{1/3.7} \right] \\[3mm] \sigma_{\mathrm{s}} = 50.8037 \sinh^{-1}\left[\left(\dfrac{Z}{2.2791 \times 10^{29}} \right)^{1/8.83} \right] \\[3mm] \sigma_{\mathrm{ss}} = 47.2266 \sinh^{-1}\left[\left(\dfrac{Z}{2.2522 \times 10^{29}} \right)^{1/8.29} \right] \\[3mm] B = \begin{cases} 12.6635 Z^{0.0058} \left(\dot{\varepsilon} = 0.01,\ 0.1\ \mathrm{s}^{-1} \right) \\ 0.2496 Z^{0.0434} \left(\dot{\varepsilon} = 1,\ 10\ \mathrm{s}^{-1} \right) \end{cases} \\[3mm] a = 2.0362 Z^{0.0175} \\ b = 3.6676 Z^{-0.0083} \\ \varepsilon_{\mathrm{p}} = 0.0068 Z^{0.0468} \\ Z = \dot{\varepsilon} \exp\left(\dfrac{392760}{RT} \right) \end{cases} \tag{13}$$

Figure 8 reveals that the predicted flow stresses agree with the measured results well. Also, the correlation coefficient can be calculated to be 0.9851 (Fig. 9), which means good prediction capability of the developed physically-based model. However, from Fig. 8, in the dynamic flow softening stage, a relatively large deviation exists when the forming temperatures are 300 and 340 °C, and strain rate is 0.01 s⁻¹. This phenomenon may be attributed to the fact that the coarsening and morphological variations of fine Mg₂Si phases precipitated at low deformation temperatures are not taken into account in the developed constitutive models.

4 Hot workability of studied Al−Si−Mg alloy

4.1 Establishment of processing map

In terms of the principle of the dynamic materials modeling (DMM) [22], power dissipater can be well applied to characterize the hot working process of alloys. Usually, the total instantaneous power dissipation (P) is composed of two parts: one refers to the dissipation energy (G content) converted into temperature rise; the other corresponds to the complementary dissipation energy (J co-content) for the microstructural evolution in the process of hot deformation. The parameter of P can be expressed by

$$P = \sigma\dot{\varepsilon} = G + J = \int_0^{\dot{\varepsilon}} \sigma \mathrm{d}\dot{\varepsilon} + \int_0^{\sigma} \dot{\varepsilon} \mathrm{d}\sigma \tag{14}$$

where $\dot{\varepsilon}$ and σ are the strain rate and flow stress, respectively.

When strain and temperature are constant, the flow stress can be described by

$$\sigma = K\dot{\varepsilon}^m \tag{15}$$

where K denotes a material constant. m denotes the coefficient of strain rate sensitivity, and can be represented by

$$m = \frac{\mathrm{d}J}{\mathrm{d}G} = \frac{\mathrm{d}(\ln \sigma)}{\mathrm{d}(\ln \dot{\varepsilon})} \tag{16}$$

J co-content can be determined from

$$J = \int_0^{\sigma} \dot{\varepsilon} \mathrm{d}\sigma = \frac{m}{m+1} \sigma\dot{\varepsilon} \tag{17}$$

For an ideal process of linear dissipation, $m=1$ and $J_{\max} = \sigma\dot{\varepsilon}/2$. The power dissipation efficiency (η) can be represented by

$$\eta = \frac{J}{J_{\max}} = \frac{2m}{m+1} \tag{18}$$

According to the theory of the maximum rate of production entropy, another dimensionless parameter (ξ), a continuum instability criterion, can be well applied to identify the occurrence of flow instabilities:
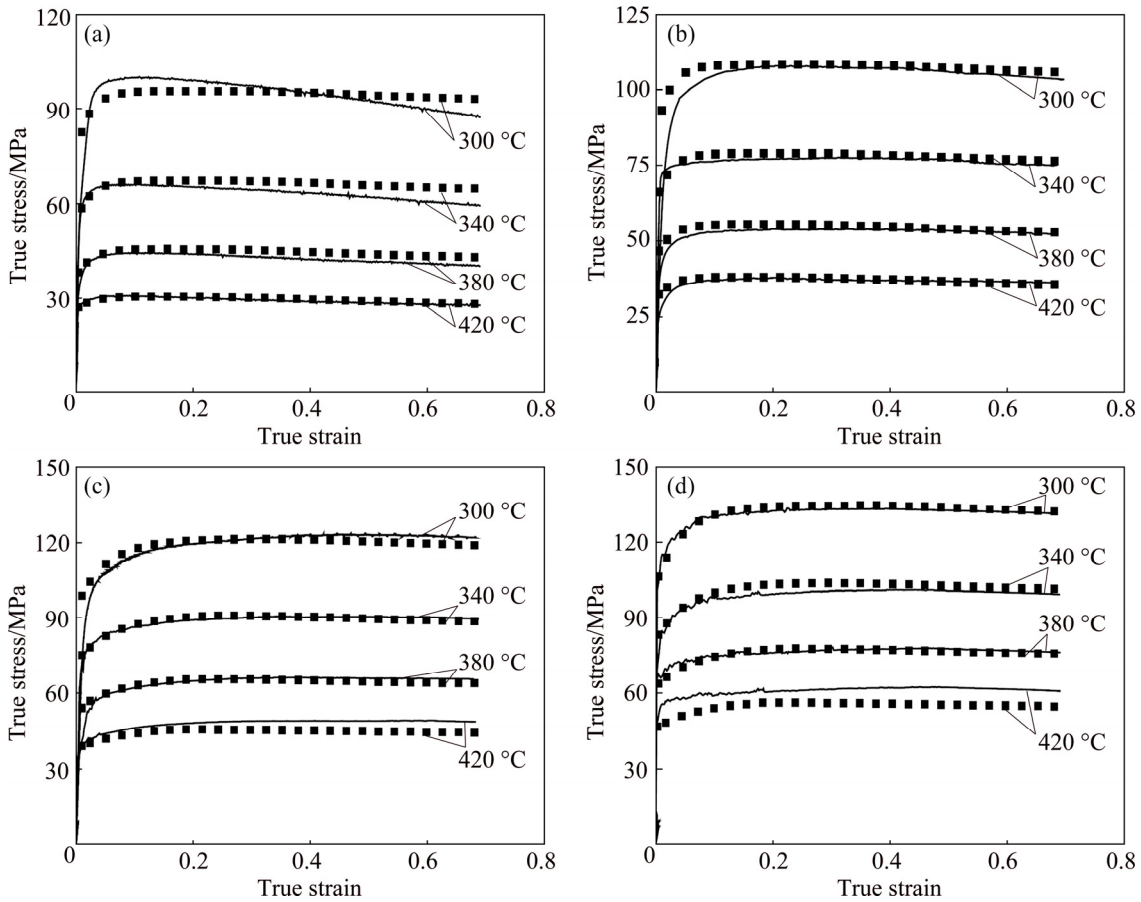
Fig. 8 Comparisons between predicted and measured flow stress curves of studied Al−Si−Mg alloy at different strain rates: (a) 0.01 s^{-1}; (b) 0.1 s^{-1}; (c) 1 s^{-1}; (d) 10 s^{-1}
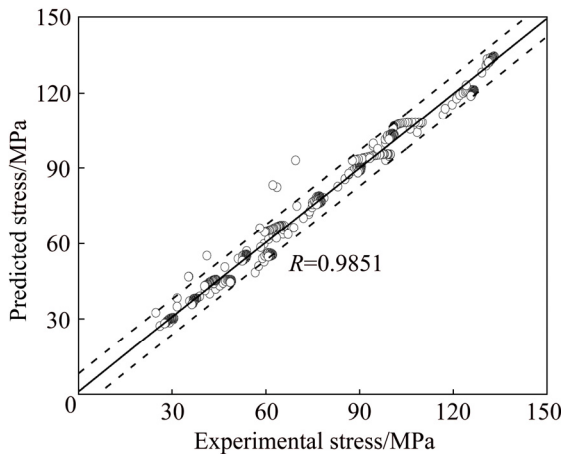

Fig. 9 Comparisons between experimental and predicted flow stresses of studied Al−Si−Mg alloy

$$\xi(\dot{\varepsilon}) = \frac{\partial \ln(\frac{m}{m+1})}{\partial (\ln \dot{\varepsilon})} + m \leq 0 \qquad (19)$$

Using the approach of three order polynomial fitting, the values of m can be easily determined from the relationship between $\ln \sigma$ and $\ln \dot{\varepsilon}$. Then, according to Eqs. (18) and (19), the values of η and ξ can be calculated, respectively.

Based on the above theory, plotting the changes of η with the deformation temperature and strain rate at a constant strain constructs the power dissipation maps. The maximum values of power dissipation efficiency do not always imply the optimal workability, since the wedge crack and flow instabilities may occur. Moreover, plotting the changes of ξ with the deformation temperature and strain rate constitutes the instability maps. The domains with negative ξ represent the instable flow and are regarded as the "unsafe" domains by shadow [37]. Then, the processing maps are constituted by superposing the power dissipation map and the instability map. In general, the optimum forming parameters are in the "safe" domains with the largest values of power dissipation efficiency [38,39].

4.2 Optimization of hot working domains

Figure 10 depicts the influence of strain on the processing maps established at 300−420 °C and 0.01− 10 s^{-1}. The "unsafe" domains are represented by the shaped areas and the contours show the values of power dissipation efficiency in the processing maps. Obviously, the instability domains are mainly located at the regions
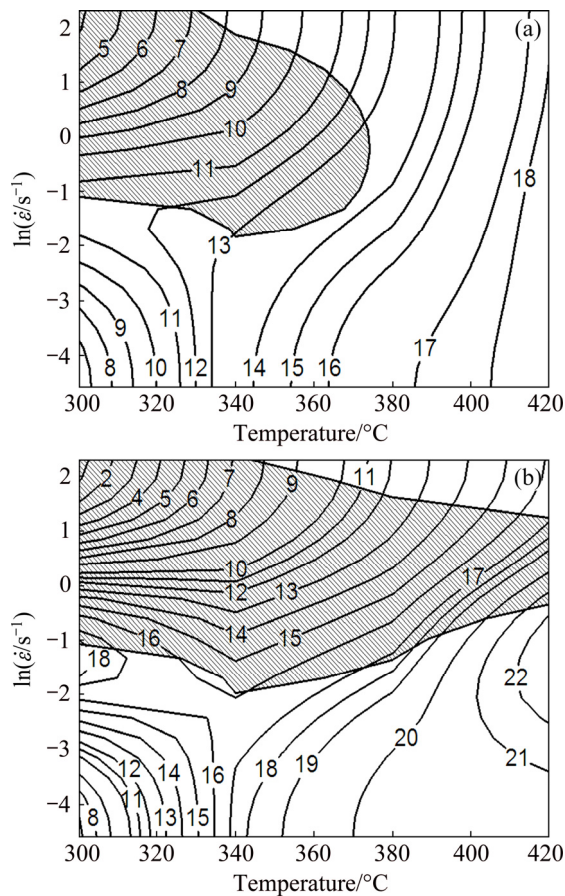
Fig. 10 Processing maps of studied Al−Si−Mg alloy at different strains: (a) 0.2; (b) 0.6

with low forming temperatures and high strain rates. When the strain is further increased, the first instability domain rapidly increases. Also, the power dissipation map shows two domains with high values of power dissipation efficiency at 305 °C, 0.26 s^{-1} and 480 °C, 0.25 s^{-1} (shown in Fig. 10(b)), which indicates that a large amount of energy are dissipated in the microstructural evolution. This is suitable for the hot forming of the studied alloy. Meanwhile, it can be clearly found that a portion of the above domain with high power dissipation efficiency shows negative instable parameter, which should be avoided [40]. Therefore, two feasible hot forming domains at the intermediate strain rate can be identified, i.e., Domain 1 with peak efficiency of approximately 0.18 appears at 300−320 °C and 0.09−0.27 s^{-1}, and Domain 2 with peak efficiency of approximately 0.23 appears at 380−420 °C and 0.03−0.28 s^{-1}. In order to further gain the optimum hot forming window, the characteristics of microstructure and hot forming mechanism in both domains are studied by optical microscope observations.

Figure 11 shows the optical microstructures of specimens deformed at the strain rate of 0.1 s^{-1} and temperatures of 300, 380 and 420 °C. Apparently, the
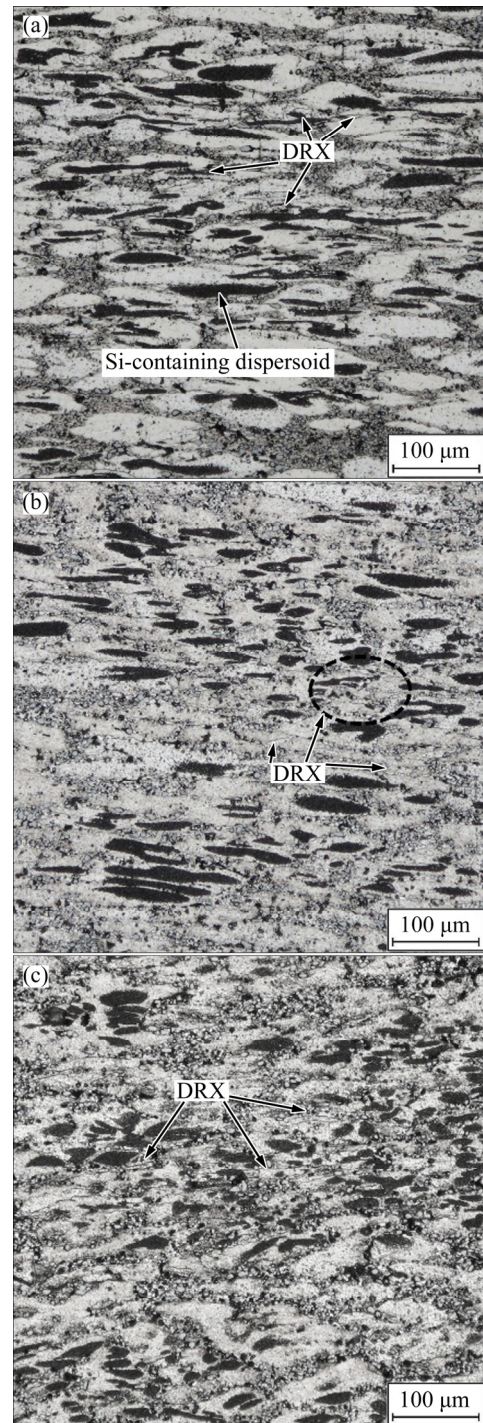

Fig. 11 Optical microstructures of studied Al−Si−Mg alloy deformed at strain rate of 0.1 s^{-1} and different temperatures: (a) 300 °C; (b) 380 °C; (c) 420 °C

grains of the deformed specimens are elongated perpendicular to the compression direction, as well as the Si-containing dispersoids in the α(Al) matrix. Meanwhile, no casting defects such as micro-cracks and pores, or adiabatic shear band, are observed. This should be the typical dynamic recovery microstructures. Therefore, the DRV is the primary softening mechanism in both domains. However, when the forming

temperature is relatively higher (Figs. 11(b) and (c)), the grains of the deformed specimen tend to be of less aspect ratio. Thus, the grain size is smaller than that at low deformation temperature (Fig. 11(a)). Moreover, a small amount of fine grains on the elongated boundaries (in Domain 1) are observed at 300 °C, 0.1 s^{-1}. This is an initiation of DRX of the studied alloy. For the sample at 420 °C, 0.1 s^{-1} (in Domain 2), the small grains begin to grow up, and are mainly distributed on the large grain boundaries. Furthermore, some fine grains inside the large grains are observed. This should be the typical microstructural characteristic of incomplete DRX, which was also discovered in other as-cast Al−Si−Mg alloy [41]. Such a phenomenon can be attributed to the relatively low peak power dissipation efficiency of the studied Al−Si−Mg alloy. Lots of investigations indicate that the completed DRX can occur for alloys during hot forming when the power dissipation efficiency is larger than 0.3 [42]. For the metals or alloys with high stacking fault energy, especially the aluminum alloys, higher power dissipation efficiency is needed for a completed DRX, because of the difficulty in dislocation entanglement and accumulation, as well as new grain nucleation [43]. As shown in Fig. 10(b), the peak power

dissipation efficiency of the studied Al−Si−Mg alloy is only 0.18 and 0.23 in domains 1 and 2, respectively. Thus, the DRV is the main hot forming mechanism of the studied Al−Si−Mg alloy. So, DRV−DRX mixture microstructures appear in Domain 2. Such a phenomenon indicates that a relatively high temperature of DRX exists for the homogenized Al−Si−Mg alloy, which has been demonstrated to be beneficial to mechanical properties of alloys at high in-service temperatures.

In general, the hot working of alloys, including the hot spinning, rolling and forging, is performed in a relatively large temperature range. The hot forming of the homogenized Al−Si−Mg alloy can be generally implemented at the tested temperatures of 300−420 °C with strain rate lower than 0.14 s^{-1} to avoid the flow instability. In addition, Domain 2 should be considered as the optimum hot working window, i.e., 380−420 °C and 0.03−0.28 s^{-1}. In this optimum hot working window, there are low energy consumption, high power dissipation efficiency and fine grains of the studied alloy.

Meanwhile, the instable flow may be attributed to the local cavity, shear band deformation, and brittle fracture of eutectic silicon phase at the low deformation temperatures and high strain rates. Figure 12 exhibits the
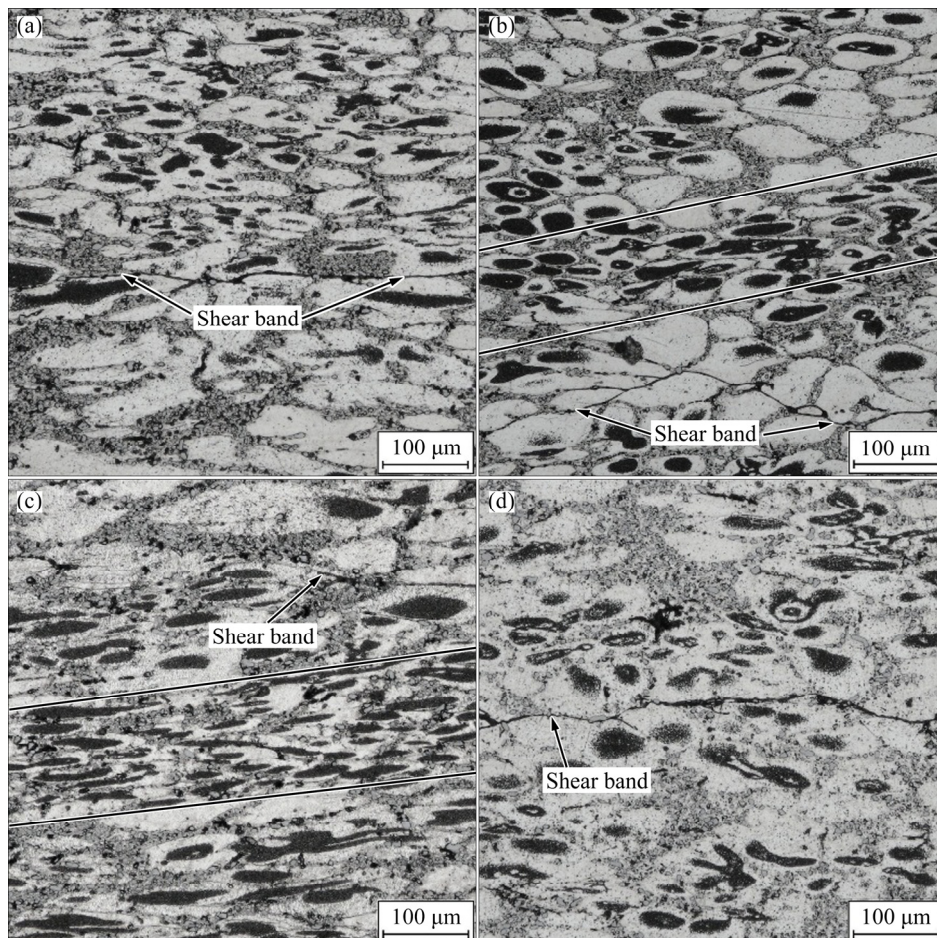

Fig. 12 Optical microstructures of studied Al−Si−Mg alloy deformed under different conditions: (a) 300 °C, 1 s^{-1}; (b) 300 °C, 10 s^{-1}; (c) 340 °C, 1 s^{-1}; (d) 340 °C, 10 s^{-1}
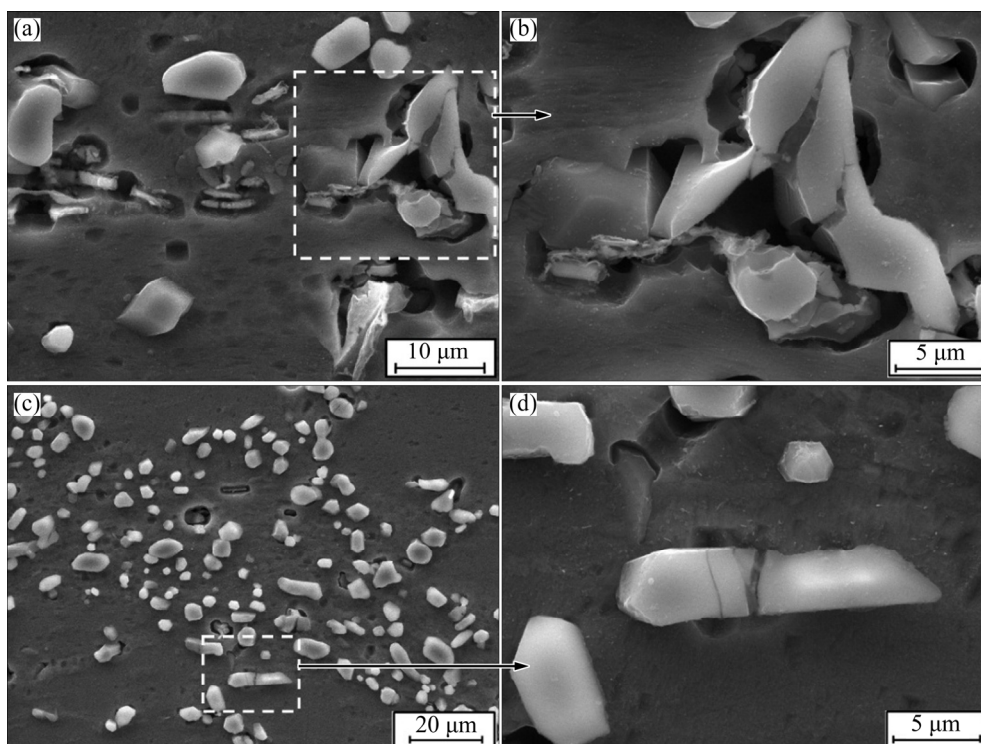
Fig. 13 SEM images of studied Al−Si−Mg alloy deformed under different conditions: (a, b) 300 °C, 10 s^{-1}; (c, d) 340 °C, 10 s^{-1}

instable flow optical microstructures of the studied Al−Si−Mg alloy compressed at the low temperatures and high strain rates. Obviously, the adiabatic shear bands appear. Furthermore, the local inhomogeneous deformation can be observed, which should be avoided in the process of hot forming. Figure 13 shows the SEM images of the studied Al−Si−Mg alloy deformed at 300−340 °C and 10 s^{-1}. It is easily found that the effects of the orientation of the initial eutectic silicon phase on its shape are significant. If the orientation is not perpendicular to the compression direction, the initial eutectic silicon phase will be distorted and snapped noticeable. Furthermore, if the size of the initial eutectic silicon phase is over a certain value, and is perpendicular to the compression direction, it is prone to fracture.

Generally, the significant differences in elastic constants of the α(Al) matrix and eutectic silicon phases lead to the strong strain incompatibility between them, which in turn easily causes the local plastic flow and larger stress concentration around silicon particles at the low forming temperatures and high strain rates [44]. Once the stress is higher than the critical value, the crack initiation happens, which finally results in the fragmentation of silicon particles. This may be the reason for the quick increment of instability domain in processing map at the low forming temperatures and high strain rates in the initial stage of deformation. The cracked eutectic silicon particles are potential cavity nucleation positions. When the strain is further increased, the cavities grow and gradually coalesce to form larger

cracks, which may finally lead to the macroscopic fracture at the low forming temperatures and high strain rates. However, because of the increase of atomic diffusion and dislocation movement, the local stress concentration around the silicon particles is reduced at high temperatures. Thus, the critical strain or stress required for the fracture of silicon particles is significantly enhanced. As a result, the hot forming at the tested temperature of 380−420 °C and strain rate of 10 s^{-1} is "safe" even the strain is increased to 0.6, as shown in Fig. 10(b).

5 Conclusions

1) The deformation temperature and strain rate strongly affect the flow stress. The flow stress can be reduced by decreasing the strain rate or increasing the deformation temperature.

2) A physically-based model is developed to predict the flow stress of Al−Si−Mg alloy. The correlation coefficient (R) between the measured and predicted stresses is 0.9851, indicating good prediction capability of the proposed constitutive model. The deformation activation energy is closely related to the pinning of dislocations from Si-containing dispersoids.

3) The deformed grains and the Si-containing dispersoids in the matrix are elongated perpendicular to the compression direction, and incomplete DRX is discovered on the elongated boundaries in domain with peak efficiency. The flow instability is mainly attributed

to the local inhomogeneous deformation, the formation of adiabatic shear band, and brittle fracture of eutectic silicon phase at the low forming temperatures and high strain rates.

4) The hot forming of the homogenized Al−Si−Mg alloy can be generally implemented at the tested temperature of 300−420 °C with strain rate lower than 0.14. 380−420 °C and 0.03−0.28 s^{-1} are selected as the optimum hot working parameters for isothermal forging.

References

[1]   LIN Y C, CHEN Xiao-min. A critical review of experimental results and constitutive descriptions for metals and alloys in hot working [J]. Materials & Design, 2011, 32(4): 1733−1759.

[2]   YANG Nan, NING Yong-quan, LIANG Hou-quan, GUO Hong-zhen, YAO Ze-kun, FU M W. Work-hardening effect and strain-rate sensitivity behavior during hot deformation of Ti−5Al−5Mo−5V−1Cr−1Fe alloy [J]. Materials & Design, 2015, 82: 84−90.

[3]   LIU Yan-xing, LIN Y C, ZHOU Ying. 2D cellular automaton simulation of hot deformation behavior in a Ni-based superalloy under varying thermal-mechanical conditions [J]. Materials Science and Engineering A, 2017, 691: 88−99.

[4]   HUANG Shu-hai, SHU Da-yu, HU Chuan-kai, ZHU Shi-feng. Effect of strain rate and deformation temperature on strain hardening and softening behavior of pure copper [J]. Transactions of Nonferrous Metals Society of China, 2016, 26(4): 1044−1054.

[5]   DEHGHAN H, ABBASI S M, MOMENI A, KARIMI T A. On the constitutive modeling and microstructural evolution of hot compressed A286 iron-base superalloy [J]. Journal of Alloys and Compounds, 2013, 564: 13−19.

[6]   MOMENI A, DEHGHANI K, EBRAHIMI G R, KAZEMI S. Developing the processing maps using the hyperbolic sine constitutive equation [J]. Metallurgical and Materials Transactions A, 2013, 44(12): 5567−5576.

[7]   LI Yu-fei, WANG Zhen-hong, ZHANG Lin-ying, LUO Chao, LAI Xin-chun. Arrhenius-type constitutive model and dynamic recrystallization behavior of V−5Cr−5Ti alloy during hot compression [J]. Transactions of Nonferrous Metals Society of China, 2015, 25(6): 1889−1900.

[8]   CHEN Dong-dong, LIN Y C, ZHOU Ying, CHEN Ming-song, WEN Dong-xu. Dislocation substructures evolution and an adaptive-network-based fuzzy inference system model for constitutive behavior of a Ni-based superalloy during hot deformation [J]. Journal of Alloys and Compounds, 2017, 708: 938−946.

[9]   LIN Y C, HE Min, CHEN Ming-song, WEN Dong-xu, CHEN Jian. Effects of initial δ phase (Ni$_3$Nb) on hot tensile deformation behaviors and material constants of a Ni-based superalloy [J]. Transactions of Nonferrous Metals Society of China, 2016, 26(1): 107−117.

[10]   GANGOLU S, RAO A G, SABIROV I, KASHYAP B P, PRABHU N, DESHMUKH V P. Development of constitutive relationship and processing map for Al−6.65Si−0.44Mg alloy and its composite with B$_4$C particulates [J]. Materials Science and Engineering A, 2016, 655: 256−264.

[11]   HAGHDADI N, ZAREI-HANZAKI A, ABEDI H R, SABOKPA O. The effect of thermomechanical parameters on the eutectic silicon characteristics in a non-modified cast A356 aluminum alloy [J]. Materials Science and Engineering A, 2012, 549: 93−99.

[12]   SINGH S K, CHATTOPADHYAY K, DUTTA P. High-temperature workability of thixocast A356 aluminum alloy [J]. Metallurgical and Materials Transactions A, 2015, 46(7): 3248−3259.

[13]   WANG S, LUO J R, HOU L G, ZHANG J S, ZHUANG L Z. Physically based constitutive analysis and microstructural evolution of AA7050 aluminum alloy during hot compression [J]. Materials & Design, 2016, 107: 277−289.

[14]   VILAMOSA V, CLAUSEN A H, BØRVIK T, HOLMEDALB B, HOPPERSTAD O S. A physically-based constitutive model applied to AA6082 aluminium alloy at large strains, high strain rates and elevated temperatures [J]. Materials & Design, 2016, 103: 391−405.

[15]   MIRZADEH H. Simple physically-based constitutive equations for hot deformation of 2024 and 7075 aluminum alloys [J]. Transactions of Nonferrous Metals Society of China, 2015, 25(5): 1614−1618.

[16]   HE An, XIE Gan-lin, YANG Xiao-ya, WANG Xi-tao, ZHANG Hai-long. A physically-based constitutive model for a nitrogen alloyed ultralow carbon stainless steel [J]. Computational Materials Science, 2015, 98: 64−69.

[17]   SENTHILKUMAR V, BALAJI A, ARULKIRUBAKARAN D. Application of constitutive and neural network models for prediction of high temperature flow behavior of Al/Mg based nanocomposite [J]. Transactions of Nonferrous Metals Society of China, 2013, 23(6): 1737−1750.

[18]   BOBBILI R, MADHU V. Constitutive modeling of hot deformation behavior of high-strength armor steel [J]. Journal of Materials Engineering and Performance, 2016, 25(5): 1829−1838.

[19]   TRIMBLE D, O'DONNELL G E. Flow stress prediction for hot deformation processing of 2024Al-T3 alloy [J]. Transactions of Nonferrous Metals Society of China, 2016, 26(5): 1232−1250.

[20]   LIN Y C, ZHANG Jun, ZHONG Jue. Application of neural networks to predict the elevated temperature flow behavior of a low alloy steel [J]. Computational Materials Science, 2008, 43(4): 752−758.

[21]   BOBBILI R, RAMAKRISHNA B, MADHU V, GOGIA A K. Prediction of flow stress of 7017 aluminium alloy under high strain rate compression at elevated temperatures [J]. Defence Technology, 2015, 11(1): 93−98.

[22]   PRASAD Y V R K, GEGEL H L, DORAIVELU S M, MALAS J C, MORGAN J T, LARK K A, BARKER D R. Modeling of dynamic material behavior in hot deformation: Forging of Ti-6242 [J]. Metallurgical and Materials Transactions A, 1984, 15(10): 1883−1892.

[23]   CEPEDA-JIMÉNEZ C M, RUANO O A, CARSÍ M, CARREÑO F. Study of hot deformation of an Al−Cu−Mg alloy using processing maps and microstructural characterization [J]. Materials Science and Engineering A, 2012, 552: 530−539.

[24]   BOBBILI R, MADHU V. An investigation into hot deformation characteristics and processing maps of high-strength armor steel [J]. Journal of Materials Engineering and Performance, 2015, 24(12): 4728−4735.

[25]   XUE Yong, ZHANG Zhi-min, LU Guang, XIE Zhi-ping, YANG Yong-biao, CUI Ya. Study on flow stress model and processing map of homogenized Mg−Gd−Y−Zn−Zr alloy during thermomechanical processes [J]. Journal of Materials Engineering and Performance, 2015, 24(2): 964−971.

[26]   CHEN Rui, XU Qing-yan, JIA Zhao-nian, LIU Bai-cheng. Precipitation behavior and hardening effects of Si-containing dispersoids in Al−7Si−Mg alloy during solution treatment [J]. Materials & Design, 2016, 90: 1059−1068.

[27]   MOMENI A, EBRAHIMI G R, FARIDI H R. Effect of chemical composition and processing variables on the hot flow behavior of leaded brass alloys [J]. Materials Science and Engineering A, 2015, 626: 1−8.

[28]   SATHEESH KUMAR S S, RAGHU T, BHATTACHARJEE P P, RAO G A, BORAH U. Strain rate dependent microstructural evolution during hot deformation of a hot isostatically processed nickel base superalloy [J]. Journal of Alloys and Compounds, 2016, 681: 28−42.

[29] LIN Y C, ZHAO Chun-yang, CHEN Ming-song, CHEN Dong-dong. A novel constitutive model for hot deformation behaviors of Ti−6Al−4V alloy based on probabilistic method [J]. Applied Physics A, 2016, 122(8): 1−9.

[30] ESTRIN Y, MECKING H. A unified phenomenological description of work hardening and creep based on one-parameter models [J]. Acta Metallurgica, 1984, 32(1): 57−70.

[31] SELLARS C M, MCTEGART W J. On the mechanism of hot deformation [J]. Acta Metallurgica, 1966, 14(9): 1136−1138.

[32] LIN Y C, WEN Dong-xu, DENG Jiao, LIU Guan, CHEN Jian. Constitutive models for high-temperature flow behaviors of a Ni-based superalloy [J]. Materials & Design, 2014, 59: 115−123.

[33] MCQUEEN H, RYAN N D. Constitutive analysis in hot working [J]. Materials Science and Engineering A, 2002, 322(1): 43−63.

[34] KONG L X, HODGSON P D, COLLINSON D C. Extrapolative prediction of the hot strength of austenitic steels with a combined constitutive and ANN model [J]. Journal of Materials Processing Technology, 2000, 102(1): 84−89.

[35] JONAS J J, QUELENNEC X, JIANG Lan, MARTIN É. The Avrami kinetics of dynamic recrystallization [J]. Acta Materialia, 2009, 57(9): 2748−2756.

[36] SOUZA P M, BELADI H, SINGH R, ROLFE B, HODGSON P D. Constitutive analysis of hot deformation behavior of a Ti₆Al₄V alloy using physical based model [J]. Materials Science and Engineering A, 2015, 648: 265−273.

[37] WEN Dong-xu, LIN Y C, CHEN Jian, DENG Jiao, CHEN Xiao-min, ZHANG Jin-long, HE Min. Effects of initial aging time on processing map and microstructures of a nickel-based superalloy [J]. Materials Science and Engineering A, 2014, 620: 319−332.

[38] HE Dao-guang, LIN Y C, CHEN Ming-song, CHEN Jian, WEN Dong-xu, CHEN Xiao-min. Effect of pre-treatment on hot deformation behavior and processing map of an aged nickel-based superalloy [J]. Journal of Alloys and Compounds, 2015, 649: 1075−1084.

[39] XU Yi, WANG Jie. Hot deformation behavior of spray forming LSHR alloy using constitutive equation and processing map [J]. Transactions of Nonferrous Metals Society of China, 2016, 26(4): 1032−1043.

[40] WEN Dong-xu, LIN Y C, LI Hong-bin, CHEN Xiao-min, LI Lei-ting, DENG Jia. Hot deformation behavior and processing map of a typical Ni-based superalloy [J]. Materials Science and Engineering A, 2014, 591: 183−192.

[41] KAI Xi-zhou, CHEN Cun, SUN Xia-fei, WANG Chun-mei, ZHAO Yu-tao. Hot deformation behavior and optimization of processing parameters of a typical high-strength Al−Mg−Si alloy [J]. Materials & Design, 2016, 90: 1151−1158.

[42] FENG Di, ZHANG Xin-ming, LIU Sheng-dan, WU Ze-zheng, TAN Qi. Rate controlling mechanisms in hot deformation of 7A55 aluminum alloy [J]. Transactions of Nonferrous Metals Society of China, 2014, 24(1): 28−35.

[43] ZHU Rui-hua, LIU Qing, LI Jin-feng, XIANG Sheng, CHEN Yong-lai, ZHANG Xu-hu. Dynamic restoration mechanism and physically based constitutive model of 2050 Al−Li alloy during hot compression [J]. Journal of Alloys and Compounds, 2015, 650: 75−85.

[44] LIAO Heng-cheng, WU Yu-na, ZHOU Ke-xin, YANG Jian. Hot deformation behavior and processing map of Al−Si−Mg alloys containing different amount of silicon based on Gleebe-3500 hot compression simulation [J]. Materials & Design, 2015, 65: 1091−1099.

锶变质 Al−Si−Mg 合金的热变形行为：本构模型与加工图

蔺永诚 [1,2,3]，骆顺存 [1,2]，姜星友 [1,2]，唐 依 [1,2]，陈明松 [1,2,3]

1. 中南大学 机电工程学院，长沙 410083；
2. 中南大学 轻合金研究院，长沙 410083；
3. 中南大学 高性能复杂制造国家重点实验室，长沙 410083

摘 要：为了研究锶变质 Al−Si−Mg 合金的热变形行为，在变形温度(300~420 °C)和应变速率(0.01~10 s⁻¹)条件下，进行了等温压缩试验。建立了一种可以准确预测流变应力的基于物理机制的流变应力本构模型。研究结果表明，降低应变速率或提高变形温度可使流变应力降低。高的变形激活能与含 Si 弥散相钉扎位错密切相关。此外，晶粒和基体中含 Si 弥散相经过热变形后沿垂直于压缩方向伸长，且处于功率耗散峰值区域，伸长晶粒晶界附近出现不完全动态再结晶。流变失稳主要归因于流变局部化、绝热剪切带的形成及共晶 Si 相的脆性断裂。最佳的热加工窗口为 380~420 °C 和 0.03~0.28 s⁻¹。

关键词：Al−Si−Mg 合金；本构模型；加工图

(Edited by Bing YANG)